

RESEARCH ARTICLE

10.1029/2018JB016174

Key Points:

- Frictional strength and stability of powdered gouges are affected by the relative amount of tectosilicates, phyllosilicates, and carbonates
- Gouges with less phyllosilicates exhibit higher healing rates
- The presence of carbonates can affect gouge frictional stability and healing

Supporting Information:

- Supporting Information S1
- Table S1

Correspondence to:

F. Zhang,
fengshou.zhang@tongji.edu.cn

Citation:

Zhang, F., An, M., Zhang, L., Fang, Y., & Elsworth, D. (2019). The role of mineral composition on the frictional and stability properties of powdered reservoir rocks. *Journal of Geophysical Research: Solid Earth*, 124, 1480–1497. <https://doi.org/10.1029/2018JB016174>

Received 3 JUN 2018

Accepted 4 FEB 2019

Accepted article online 5 FEB 2019

Published online 27 FEB 2019

The Role of Mineral Composition on the Frictional and Stability Properties of Powdered Reservoir Rocks

Fengshou Zhang^{1,2} , Mengke An^{1,2}, Lianyang Zhang³, Yi Fang⁴ , and Derek Elsworth^{5,6} 

¹Key Laboratory of Geotechnical and Underground Engineering of Ministry of Education, Tongji University, Shanghai, China, ²Department of Geotechnical Engineering, Tongji University, Shanghai, China, ³Department of Civil Engineering and Engineering Mechanics, University of Arizona, Tucson, AZ, USA, ⁴Institute for Geophysics, Jackson School of Geosciences, The University of Texas at Austin, Austin, TX, USA, ⁵Department of Energy and Mineral Engineering, EMS Energy Institute and G3 Center, The Pennsylvania State University, University Park, PA, USA, ⁶Department of Geosciences, The Pennsylvania State University, University Park, PA, USA

Abstract The growing hazard of induced seismicity driven by the boom in unconventional resources exploitation is strongly linked to fault activation. We perform laboratory measurements on simulated fault gouges comprising powdered reservoir rocks from major oil and gas production sites in China, to probe the control of mineral composition on fault friction and stability responses during reservoir stimulation. Double direct shear experiments were conducted on gouges with phyllosilicate content ranging from 0 to 30 wt.% and grain sizes <150 μm , at constant normal stresses of 10–40 MPa and conditions of room temperature and water saturation. The velocity step and slide-hold-slide sequences were employed to evaluate frictional stability and static healing, respectively. Results indicate that the mineralogy of the gouges exhibit a strong control on the frictional strength, stability, and healing. Phyllosilicate-rich samples show lower frictional strength μ and higher values of $(a - b)$, promoting stable sliding. For the gouges studied, the frictional strength decreases monotonically with increasing phyllosilicate content, and a transition from velocity weakening to velocity strengthening behavior is evident at 15 wt.% phyllosilicates. Intermediate healing rates are common in gouges with higher content of phyllosilicates, with high healing rates predominantly in phyllosilicate-poor gouges. As an indispensable component in reservoir rocks, the carbonates are shown to affect both the frictional stability and healing response. These findings can have important implications for understanding the effects of mineralogy on fault behavior and induced seismic potential in geoenvironmental activities, particularly in reservoirs in China.

1. Introduction

Induced seismicity and fault reactivation have become an important concern in anthropogenic activities of unconventional resource recovery, geothermal reservoir stimulation, CO₂ sequestration, and radioactive waste disposal (Ellsworth, 2013; Guglielmi et al., 2015; Majer et al., 2007; Shapiro et al., 2006; Walsh & Zoback, 2015), including contributions from hydraulic fracturing. The rapid increase in moderate-magnitude seismic events in western Canada as well as the central United States is highly correlated with the activation of preexisting faults induced by hydraulic fracturing and wastewater disposal (Atkinson et al., 2016; Bao & Eaton, 2016). Thus, illuminating underlying mechanisms of fault instability in reservoir systems is important in seismic hazard assessment and regulation during the lifetime of such energy-related activities. Frictional properties, primarily the frictional strength, strength evolution with slip velocity and history (velocity and state dependence), and frictional healing and creep relaxation (time dependence) are of great importance in defining the seismic behavior of major faults.

Many previous experimental studies have explored the frictional behavior of tectonic faults using both simulated and natural fault gouges spanning ranges of humidity and temperature. Table 1 also summarizes experimental conditions for friction and stability investigations of reservoir rocks in recent years. This work generally focuses on single or paired groups of phyllosilicate, tectosilicate, and carbonate minerals. Phyllosilicate minerals, such as smectite, illite, kaolinite, chlorite, biotite, and talc, are important components that control fault evolution in shallow and crustal faults and impart weakness in tectonic

Table 1
List of Experimental Conditions for Friction and Stability Investigations of Reservoir Rocks in Recent Years

Gouges	Stress condition	Humidity condition	Temperature condition	References
Caprock, reservoir rock, and the two mixtures in North Sea reservoir	Effective normal stress of 35 MPa	(1) dry, (2) dry pressurized with supercritical CO ₂ , (3) brine saturated, and (4) brine saturated pressurized with supercritical CO ₂	~115 °C	Samuelson and Spiers (2012)
Shale reservoir rocks from Barnett, Haynesville, and Eagleford reservoir	Normal stresses of 15 and 45 MPa	Ambient humidity	Room temperature	Kohli and Zoback (2013)
Unexposed and CO ₂ -exposed sandstone, and CO ₂ -exposed carbonate-rich fault rock in a natural CO ₂ reservoir	Effective normal stress of 5–90 MPa	Lab dry or wet	20–100 °C	Bakker et al. (2016)
Reservoir rocks in Newberry Geothermal reservoir	Normal stresses of 15 and 45 MPa	Water saturated	Room temperature	Fang et al. (2016)
Caprock and reservoir rock at the Groningen gas field	Effective normal stress of 40 MPa	Saturated with pure water, NaCl solutions, and mixed chloride brine	100 °C	Hunfeld et al. (2017)

faults (Crawford et al., 2008; Carpenter et al., 2011; Lockner et al., 2011; Lu & He, 2014; Saffer & Marone, 2003; Tesei et al., 2012). A common feature of phyllosilicate-rich fault gouges is that they exhibit low frictional strength and promote velocity strengthening behavior and related aseismic reactivation at room temperature (Carpenter et al., 2009; Ikari et al., 2009; Niemeijer et al., 2010). This is primarily attributed to the behavior of the layer-structured phyllosilicate minerals that minimize the effects of interlocking and dilation and inhibit stick slip (Morgan & Boettcher, 1999; Numelin et al., 2007; Tembe et al., 2010). Conversely, samples containing mostly tectosilicate minerals (mainly quartz and feldspar) exhibit high frictional strength. The observed velocity weakening behavior in tectosilicate-rich samples is manifest by an abundance of unstable and dynamic stick-slip events (Blanpied et al., 1995; Samuelson et al., 2009; Takahashi et al., 2007). Another dominant mineral group, that of carbonates, is commonly found in crustal faults and generally exhibits complex frictional behavior with response to different normal stresses, temperatures and shearing velocities (Carpenter, Collettini, et al., 2016; Scuderi et al., 2013; Verberne et al., 2013, 2015). Compared with simulated or synthetic fault gouge, the frictional properties of natural rocks or natural fault gouge can better represent the field geological conditions and more appropriately reflect the sliding behavior of natural faults. Gouges from powdered natural rocks or faults can generally be idealized as mixtures of these three primary mineral groups (Ikari et al., 2014; Kohli & Zoback, 2013; Zhang & He, 2013) namely, phyllosilicates, tectosilicates, and carbonates. Thus, frictional, stability, and healing properties of powdered natural rocks may be examined through the prism of these three principal components (Fang et al., 2016; Tesei et al., 2012).

Significant effort has been applied to study the effects of mineralogy on frictional properties of fault gouges contributing to tectonic earthquakes with less attention applied to those in reservoirs that are implicated in reactivation related to induced seismicity (Bakker et al., 2016; Hunfeld et al., 2017; Samuelson & Spiers, 2012). Since the shale-gas boom and the expansion of hydraulic fracturing for unconventional resources, injection-induced seismicity related to wastewater disposal has received widespread attention (Bao & Eaton, 2016; Keranen et al., 2014; Yeck et al., 2017). Some states and areas in the United States have promulgated laws and regulations to limit the types and rates of injected fluids and injection pressures to reduce the risk of induced seismicity (Rosen, 2015; Schupp & Drive, 2017). It is recognized that the massive injection of fluids at high rates is principally responsible for the growth in induced earthquakes (Hincks et al., 2018; Schultz et al., 2018). However, the mineralogy of the fault gouges and their frictional properties are key parameters that control the potential and type of failure of the preexisting faults (Vrolijk & van der Pluijm, 1999). Therefore, it is necessary to correlate the frictional properties of reservoir rocks with the potential for induced seismicity during reservoir stimulation.

Although a majority of experimental studies have evaluated the effects of mineralogy on the frictional properties of tectonic faults, few have examined the response of natural reservoir rocks that may be implicated in

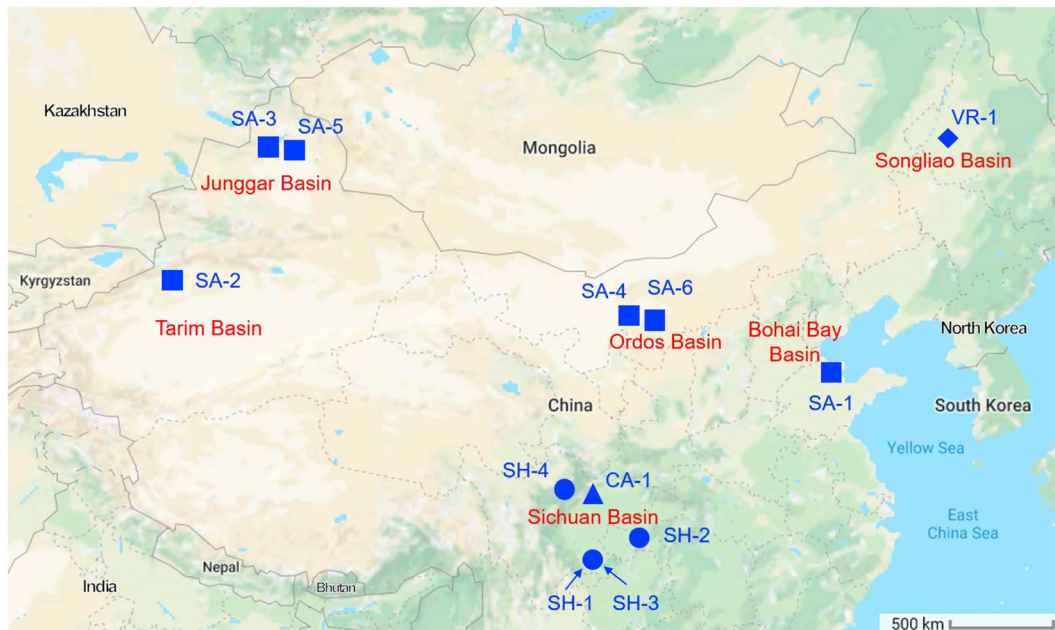


Figure 1. The distribution of major oil and gas production sites and the studied reservoir rocks in China. The words in red indicate the major oil and gas production sites in China. The blue squares, circles, triangles, and diamonds represent sandstone, shale, carbonate, and volcanic rock, respectively.

fluid-injection-induced seismicity. Likewise, there is a dearth of information on the role of mineralogy on frictional healing and relaxation (Carpenter, Colletini, et al., 2016; Chen et al., 2015a, 2015b; Karner et al., 1997; Tesei et al., 2012), which are vital in assessing strength recovery and event recurrence during repeated dynamic slip and afterslip behavior. At the same time, obtaining the friction data for reservoir rocks in China attaches great importance in assessing the seismic potential in future geoenvironmental activities. Hence, the following reports friction experiments performed on natural reservoir rocks from major oil and gas production sites of China (Figure 1). These provide a comprehensive evaluation of stability potential of faults during stimulation, with a primary investigation on the effects of mineralogy, especially phyllosilicate minerals, on frictional strength, rate dependence, and frictional healing under water-saturated conditions and at room temperature.

2. Experimental Methods

2.1. Sample Preparation

We collected six lithologies of sandstone, four shales, one carbonate, and one volcanic rock from various major oil and gas production sites in China. These include the Sichuan, Tarim, Junggar, Songliao, Bohai Bay, and Ordos Basins, as shown in Figures 1 and 2. Half of the rock samples were sourced from vertical boreholes at depths between 1,800 and 5,200 m, with the remainder recovered from outcrops. After removing all surface impurities, all rock samples were crushed and sieved to a particle size $<150\ \mu\text{m}$ to simulate fault gouge. The powdered rocks were dried at $50\ ^\circ\text{C}$ for ~ 12 hr to remove preexisting moisture before all samples were uniformly water saturated. Mineral compositions were determined by X-ray diffraction (XRD) with the results presented in Table 2. The XRD analysis for reservoir rocks were performed on the X-ray diffractometer (Rigaku D/max-rA). The quantitative XRD data were obtained using the standards “Analysis method for clay minerals and non-clay minerals by the X-ray diffraction” (National Energy Administration of China, 2010). The procedures for obtaining XRD data are as follows. The reservoir rocks were first crushed and sieved to pass through a 200-mesh sieve. Then, the rock powders were uniformly filled in a sealed groove within the X-ray diffractometer to obtain the diffraction spectrum. Finally, the data obtained from the X-ray diffractometer were analyzed according to the standards (National Energy Administration of China, 2010). The quantitative mineral contents were calculated based on the method described in Chung (1973). To ensure the accuracy of the experimental data, all XRD analysis in this

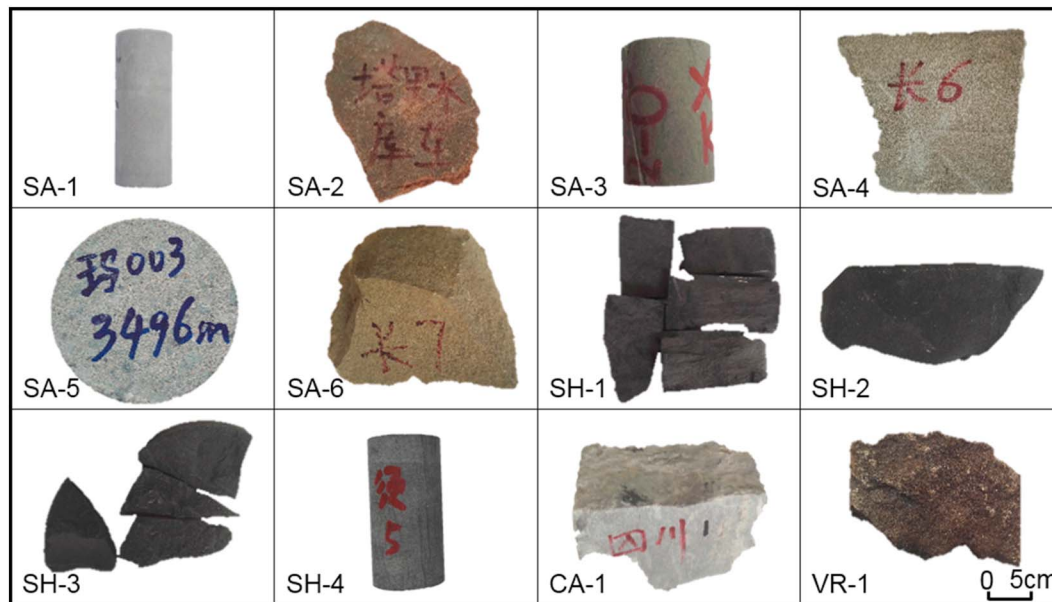


Figure 2. Reservoir rock samples for friction tests. From left to right and top to bottom: Sandstone-1 to Sandstone-6, Shale-1 to Shale-4, Carbonate-1, and Volcanic Rock-1.

work was carried out by the Micro Structure Analytical Laboratory at Peking University, China. Typical minerals include white mica, chlorite, quartz, feldspar, calcite and dolomite. In addition, pyrite was present as trace in the Longmaxi shale.

2.2. Testing Procedure

The apparatus for friction tests is located in the Key Laboratory of Geotechnical and Underground Engineering of Ministry of Education, Tongji University. This apparatus can apply horizontal and vertical loads and is especially suitable for rock compression, shear, and creep test. The main frame of the apparatus comprises horizontal and vertical loading frames. The load cell was installed on the upper and left beam for horizontal and vertical loading configurations, respectively (shown in Figure 3). The maximum vertical and horizontal force is 100 kN, with the precision of 0.5 kN. The sampling frequency of the load cell and grating displacement transducer is 100 Hz. The main frame of the apparatus was controlled by the EDC222 digital controller that was designed and manufactured by Doli, Germany. The apparatus sets the experimental

Table 2
Mineral Compositions (wt.%) of Reservoir Rock Samples Determined by X-Ray Diffraction

Sample	Depth	Location	Formation	Mc ^a	Chl	Qtz	Alb	Ort	Cal	Dol	Pyr
SA-1 ^b	3,500 m	Bohai Bay Basin	Shahejie	7	1	33	13	5	8	33	—
SA-2	Outcrop	Tarim Basin		8	2	57	19	8	6	—	—
SA-3	5,200 m	Junggar Basin	Jiamuhe	7	5	53	22	7	6	—	—
SA-4	Outcrop	Ordos Basin	Yanchang	10	4	42	20	9	15	—	—
SA-5	3,496 m	Junggar Basin	Sangonghe	12	5	47	26	10	—	—	—
SA-6	Outcrop	Ordos Basin	Yanchang	13	4	30	13	6	30	4	—
SH-1	Outcrop	Sichuan Basin	Longmaxi	10	—	44	1	1	19	23	2
SH-2	Outcrop	Sichuan Basin	Longmaxi	16	2	39	7	3	23	6	4
SH-3	2,200 m	Sichuan Basin	Longmaxi	18	5	45	10	5	9	4	4
SH-4	3,300 m	Sichuan Basin	Xujiahe	16	10	50	12	2	6	4	—
CA-1	Outcrop	Sichuan Basin	Jialingjiang	—	—	—	—	—	—	100	—
VR-1	1,862 m	Songliao Basin	Yingcheng	—	4	53	36	7	—	—	—

^aMc: white mica, Chl: chlorite, Qtz: quartz, Alb: albite, Ort: orthoclase, Cal: calcite, Dol: dolomite, and Pyr: pyrite. ^bSA: sandstone, SH: shale, CA: carbonate, VR: volcanic rock.

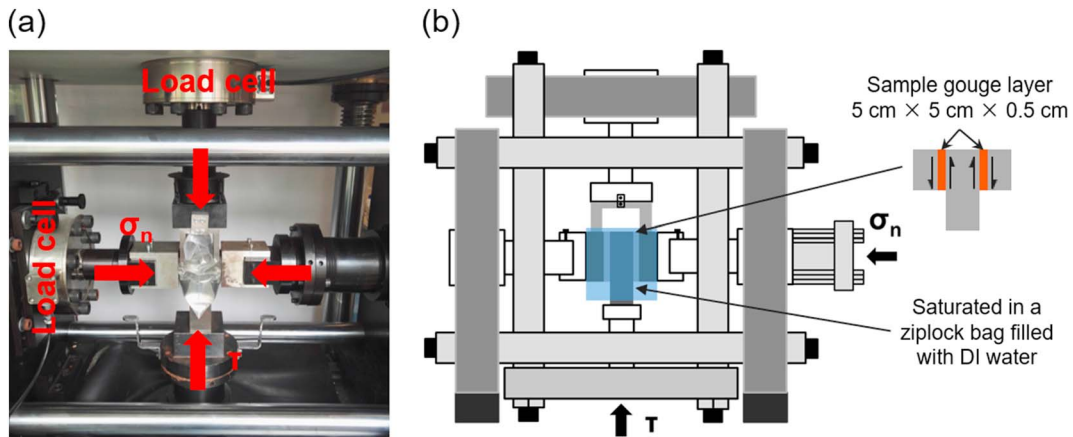


Figure 3. Static high-precision biaxial loading apparatus in double direct shear configuration. (a) Photograph and (b) schematic.

parameters and collects and processes the experimental data separately by computer. The EDC222 digital controller and the computer are connected by the network cable to control the ensemble apparatus. The force applied to the steel blocks and the normal and shear displacements were measured through the load cell and high-precision grating displacement transducer. We have calibrated the precision of the load cell and the displacement transducer before conducting the friction experiments. The load cells were calibrated through a standard load cell calibrator offered by the manufacturer. The grating displacement transducer was calibrated by the high-precision displacement calibrator.

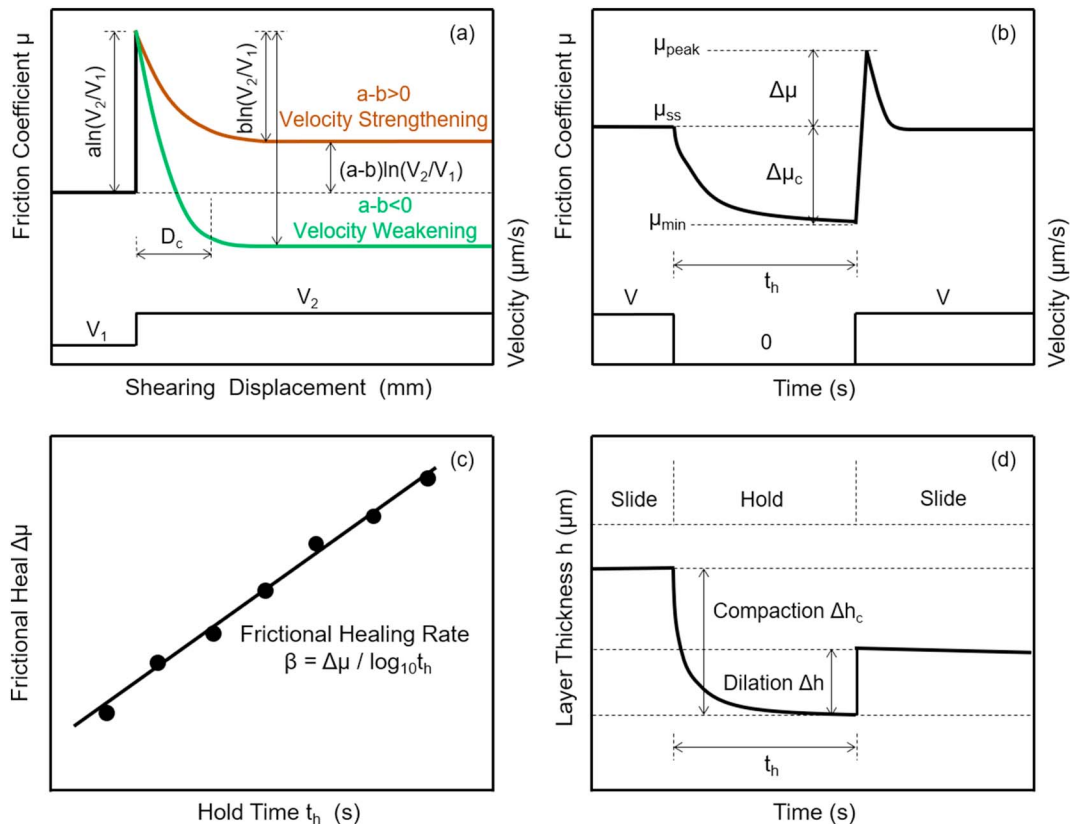


Figure 4. Schematic illustration of the idealized response of (a) velocity stepping tests and (b) slide-hold-slide tests. Example determinations of (c) frictional healing rate β and (d) frictional compaction Δh_c and dilation Δh .

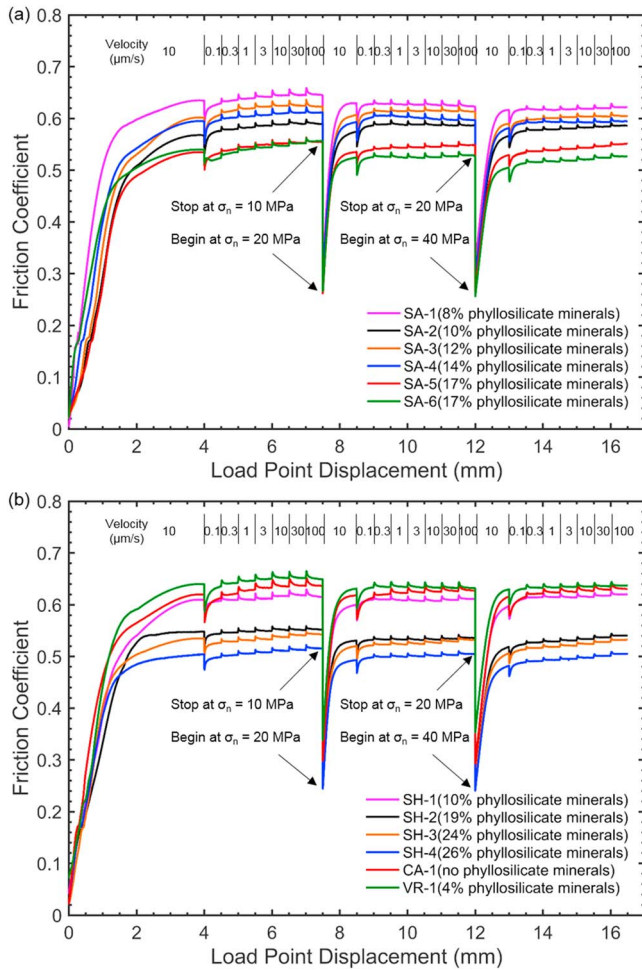


Figure 5. Evolution of friction coefficient with load point displacement in velocity stepping tests at normal stresses of 10, 20, and 40 MPa for (a) sandstone and (b) shale, carbonate, and volcanic rock.

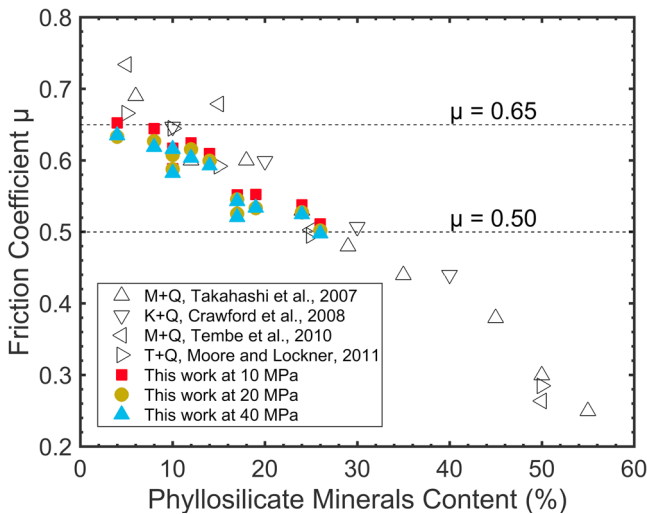


Figure 6. The relationship between friction coefficient and phyllosilicate content at normal stresses of 10, 20, and 40 MPa. The hollow triangles indicate experimental results obtained from previous studies and Q, M, K, and T represent quartz, montmorillonite, kaolinite, and talc, respectively.

All friction measurements were made in double direct shear according to a predefined shearing velocity schedule (Figure 3). The apparatus comprises three stainless steel platens grooved perpendicular to the shearing direction (1-mm width and 0.8-mm height) to act as an external loading of a fault surface that sandwich two layers (5-mm-thick natural rock powder) of simulated fault gouge. The central stainless steel block measures 10 cm × 5 cm × 3 cm (length × width × height) and the two outer blocks have dimensions of 5 cm × 5 cm × 2 cm (length × width × height). Thus, a constant contact area of 25 cm² can be maintained throughout the entire friction test. In each experiment a leveling block and balance were used to ensure both flat and parallel fault surfaces and identical mass and compactness of the two layers of fault gouge (Frye & Marone, 2002). Note that, different from many biaxial loading apparatuses, the shear load of was applied by the upward motion of the lower vertical piston (Figure 3b). A U-shaped steel block on the upper vertical piston supported the two outer steel blocks.

At the initiation of each test, the sample gouge layer was fixed on the loading platform by applying a small normal stress. The sample was then saturated with DI water contained in a ziplock bag for at least 4 hr until the simulated fault gouge was fully saturated (Frye & Marone, 2002; Scuderi et al., 2014).

Both velocity stepping and slide-hold-slide tests were performed to respectively explore the velocity dependence and frictional healing of fault gouge under water-saturated conditions at room temperature (about 25 °C). In the velocity stepping tests, a normal stress of 10 MPa was first applied in the horizontal direction with the shear load applied through a prescribed constant velocity of 10 μm/s. When the shearing displacement reached 4.0 mm and a steady state friction regime achieved, the shearing velocity was incrementally increased between 0.1, 0.3, 1, 3, 10, 30, and 100 μm/s until reaching a shear displacement of ~7.5 mm. The shear displacement during each velocity step was ~0.5 mm. Next, the normal stress was incrementally increased to 20 MPa, the samples sheared at 0.1 μm/s until ~8.5-mm cumulative shear offset and the velocity then again stepped from 0.1 to 100 μm/s until ~12.0-mm offset. Finally, the normal stress was incrementally increased to 40 MPa, and the velocity stepping repeated as in the prior two cycles until an offset of ~16.5 mm was attained. The slide-hold-slide tests were performed with a constant shearing velocity of 10 μm/s applied throughout the entire testing process. The shearing load was held for 1, 3, 10, 30, 100, 300, and 1,000 s between every 0.5 mm of shear displacement under the different normal stresses.

2.3. Data Analysis

In our experiments, the cohesion is ignored and the friction coefficient μ is typically calculated as the ratio of shear stress τ to normal stress σ_n . Rate-and-state friction (RSF; Dieterich, 1978, 1979; Ruina, 1983) theory is employed to analyze the velocity dependence of rock friction. Because some of our experimental results are better fitted by the twin state variable of the RSF law, we choose to invert for the friction parameters by directly incorporating the twin state variable. In the theory of twin state variable, the RSF law defines the friction coefficient μ as (Carpenter, Ikari, & Marone, 2016; Ikari, Niemeijer, et al., 2011; Marone, 1998)

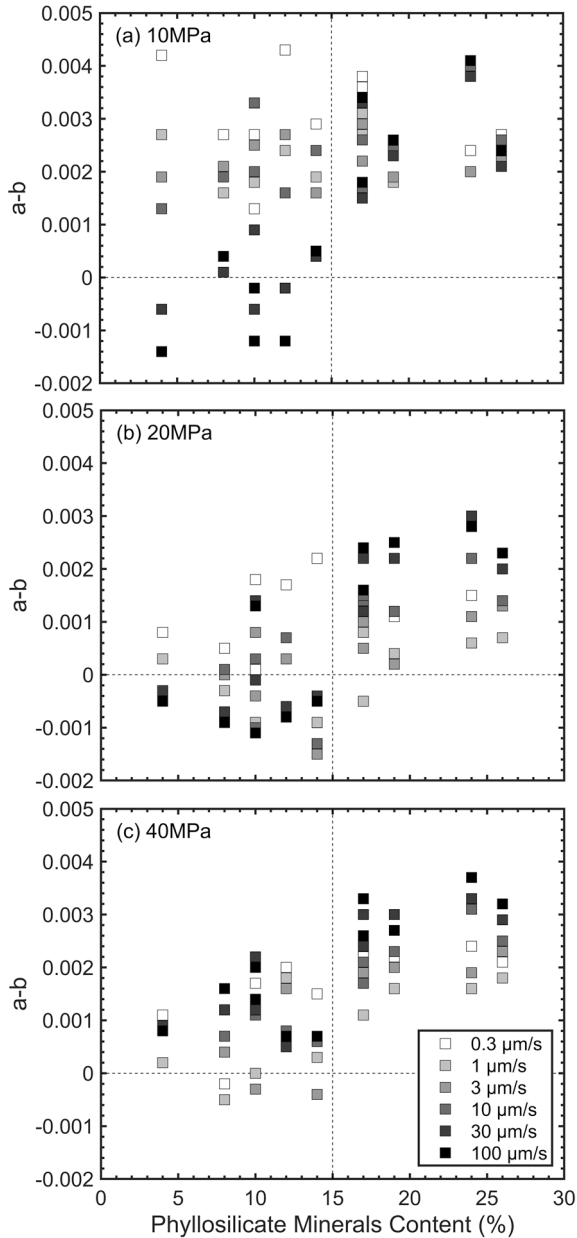


Figure 7. Velocity dependence of frictional sliding at normal stresses of (a) 10, (b) 20, and (c) 40 MPa. The legend shows the poststep velocity.

friction coefficient after hold. In contrast, the frictional relaxation ($\Delta\mu_c$) is typically determined by the steady state friction coefficient (μ_{ss}) subtracting the minimum friction coefficient during the hold, expressed by

$$\Delta\mu = \mu_{\text{peak}} - \mu_{\text{ss}} \quad (5)$$

$$\Delta\mu_c = \mu_{\text{ss}} - \mu_{\text{min}} \quad (6)$$

The rates of frictional healing (β) and relaxation (β_c) are a function of the logarithm of hold time, shown in Figure 4c, and defined as

$$\beta = \Delta\mu / \log_{10} t_h \quad (7)$$

$$\beta_c = \Delta\mu_c / \log_{10} t_h \quad (8)$$

$$\mu = \mu_0 + a \ln\left(\frac{V_2}{V_1}\right) + b_1 \ln\left(\frac{V_1\theta_1}{D_{c1}}\right) + b_2 \ln\left(\frac{V_1\theta_2}{D_{c2}}\right) \quad (1)$$

$$\frac{d\theta_i}{dt} = 1 - \frac{V_1\theta_i}{D_{ci}}, i = 1, 2 \quad (2)$$

where μ_0 denotes the friction coefficient before a velocity step (at velocity V_1); μ indicates the friction coefficient after a velocity step (at velocity V_2); a , b_1 , and b_2 are dimensionless friction parameters describing the direct and evolutionary effects caused by the step change of shearing velocity (Paterson & Wong, 2005; Tembe et al., 2010); θ_1 and θ_2 are state variables that scale with the contact of asperities and change with the time and slip history (Dieterich, 1978, 1979; Ruina, 1983); and D_{c1} and D_{c2} are critical slip displacements which represent the history of friction from the past state to a new steady state and are associated with surface contact conditions (Marone & Kilgore, 1993). For the velocity step tests, the friction parameter ($a - b$) is calculated by

$$a - b = \frac{\Delta\mu_{ss}}{\Delta \ln V} \quad (3)$$

where b is the friction parameter and calculated by $b = b_1 + b_2$ in the twin state variable RSF law, $\Delta\mu_{ss}$ represents the change of steady state friction coefficient upon an instant change in velocity from V_1 to V_2 . A positive value of ($a - b$) indicates velocity strengthening behavior, promoting stable and aseismic slip, whereas fault gouge with a negative value of ($a - b$) exhibits velocity weakening behavior and may produce unstable (seismic) slip. The response of the idealized RSF law is shown in Figure 4a. The friction parameter ($a - b$) and other friction constitutive parameters were obtained through inverse modeling (Blanpied et al., 1998; Reinen & Weeks, 1993). The coupled formulation of the RSF law with the stiffness of the testing apparatus is expressed by

$$\frac{d\mu}{dt} = K (V - V_{lp}) \quad (4)$$

where K describes the stiffness of the testing apparatus and the fault system, and V and V_{lp} are the true velocity and load point velocity of the fault sample (Reinen & Weeks, 1993; Saffer & Marone, 2003). The value of K was identified by performing unload-reload experiments, as described in Leeman et al. (2016).

The idealized response of slide-hold-slide tests during one hold is shown in Figure 4b. The frictional healing ($\Delta\mu$) is defined as the difference between the steady state friction coefficient (μ_{ss}) before hold and the peak

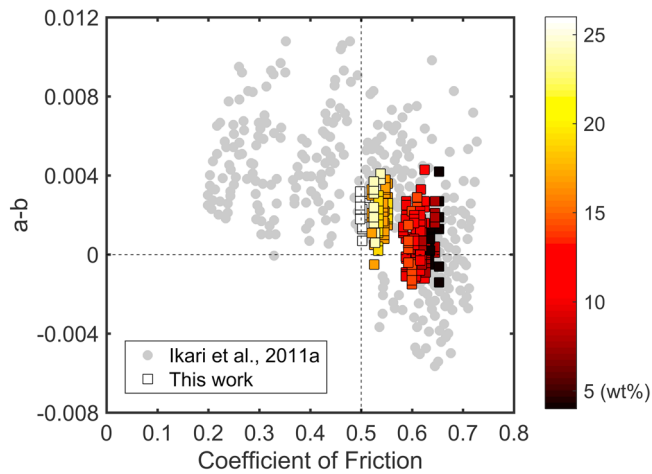


Figure 8. Comparison of friction parameter ($a - b$) with previous studies. The gray circles are adapted from Ikari, Marone, et al. (2011), and the color bar indicates the phyllosilicate content.

where t_h is the hold time during the slide-hold-slide tests. In addition, the changes of fault gouge layer thickness during slide-hold-slide tests, defined as either compaction Δh_c or dilation Δh , are important parameters to characterize frictional healing (Beeler & Tullis, 1997; Carpenter, Colletini, et al., 2016). Compaction Δh_c is defined as the layer thickness before hold subtracting the thickness at the end of hold and the dilation Δh is the difference between the thickness upon reslide relative to that at the end of the hold, as shown in Figure 4d.

3. Results

3.1. Frictional Strength and Frictional Stability

In the evaluation of results, we group the behavior of similar crystal structures into principal mineralogic groups, that is, phyllosilicates (mainly clay minerals), tectosilicates (including quartz and feldspar), and carbonates (mostly calcite and dolomite). For each experiment, the frictional strength can be represented by the value of the friction coefficient, defined as $\mu = \tau/\sigma_n$. The friction-load point displacement curves for all shearing experiments under normal stresses of 10, 20, and 40 MPa are shown in

Figure 5. Each test exhibits a similar linear increase in friction followed by slip strengthening behavior until a steady friction state is achieved at a shear offset of 4.0 mm. We measure the steady state friction coefficient at shear offsets of 5.75, 10.25, and 14.75 mm at normal stresses of 10, 20, and 40 MPa for each experiment (Table S1 in the supporting information). Figure 6 shows the evolution of the friction coefficient as a function of phyllosilicate content at different normal stresses. The friction coefficient for all samples ranges from 0.50 to 0.65 and decreases monotonically with an increase in phyllosilicate content. This is consistent with previous studies on both synthetic and simulated fault gouge (Crawford et al., 2008; Moore & Lockner, 2011; Takahashi et al., 2007; Tembe et al., 2010). The frictional strength at normal stresses of 20 and 40 MPa is typically slightly lower than that at 10 MPa.

The friction constitutive parameter ($a - b$) is a key index for assessing frictional stability and differentiating between stable and potentially unstable sliding behaviors of faults. The relationship between the friction constitutive parameter ($a - b$; Table S2) and phyllosilicate mineral content and poststep velocity are depicted in Figure 7. The measured values of ($a - b$) increase with an increase in phyllosilicate content. A transition from velocity weakening behavior ($a - b < 0$) to velocity strengthening behavior ($a - b > 0$) is observed at ~15 wt.% phyllosilicate content at normal stresses of 10, 20, and 40 MPa. From Figure 7, it is apparent that the magnitudes of ($a - b$) are in the range -0.002 to 0.003 at 20 MPa and, lower than those at 10 and 40 MPa. This implies that the normal stress influences the values of ($a - b$). Ikari et al. (2007, 2009) also noted that in clay-rich fault gouge, the magnitude of ($a - b$) is affected by the effective normal stress. In contrast, the results on shale reservoir rocks reported by Kohli and Zoback (2013) demonstrated that the values of ($a - b$) for natural rock powders are insensitive to normal stress. The relationships between magnitudes of ($a - b$) and friction coefficient and phyllosilicate mineral content are evaluated, as depicted in Figure 8. We observe a transition from stable ($a - b > 0$) to potentially unstable sliding ($a - b < 0$) with a friction coefficient of 0.55, similar to the results of Ikari, Marone, and Saffer (2011) and Kohli and Zoback (2013). However, due to the narrow range (0–30 wt.%) of phyllosilicate contents, the measured friction coefficient in this work does not cover the wide range between 0.2 and 0.8 as in previous studies (Crawford et al., 2008; Moore & Lockner, 2011; Takahashi et al., 2007; Tembe et al., 2010).

As a result of the broad range of velocity steps from 0.1 to 100 $\mu\text{m/s}$, it is of particular importance to examine the dependence of ($a - b$) on shearing velocity, as stable sliding behavior can be driven to unstable under high shearing velocities (Boatwright & Cocco, 1996). In Figure 7, mixtures containing <15 wt.% phyllosilicates exhibit some velocity strengthening behavior at lower velocities at normal stresses of 10 and 20 MPa. For samples containing <15 wt.% phyllosilicate minerals, ($a - b$) decreases with an increase in shearing velocity and unstable sliding occurs at high shearing velocities at normal stresses of 10 and 20 MPa, revealing the potential weakening of faults at higher shearing velocities (Boulton et al., 2017; Togo et al., 2016). Conversely, for samples containing >15 wt.% phyllosilicate, the values of ($a - b$) increase with higher

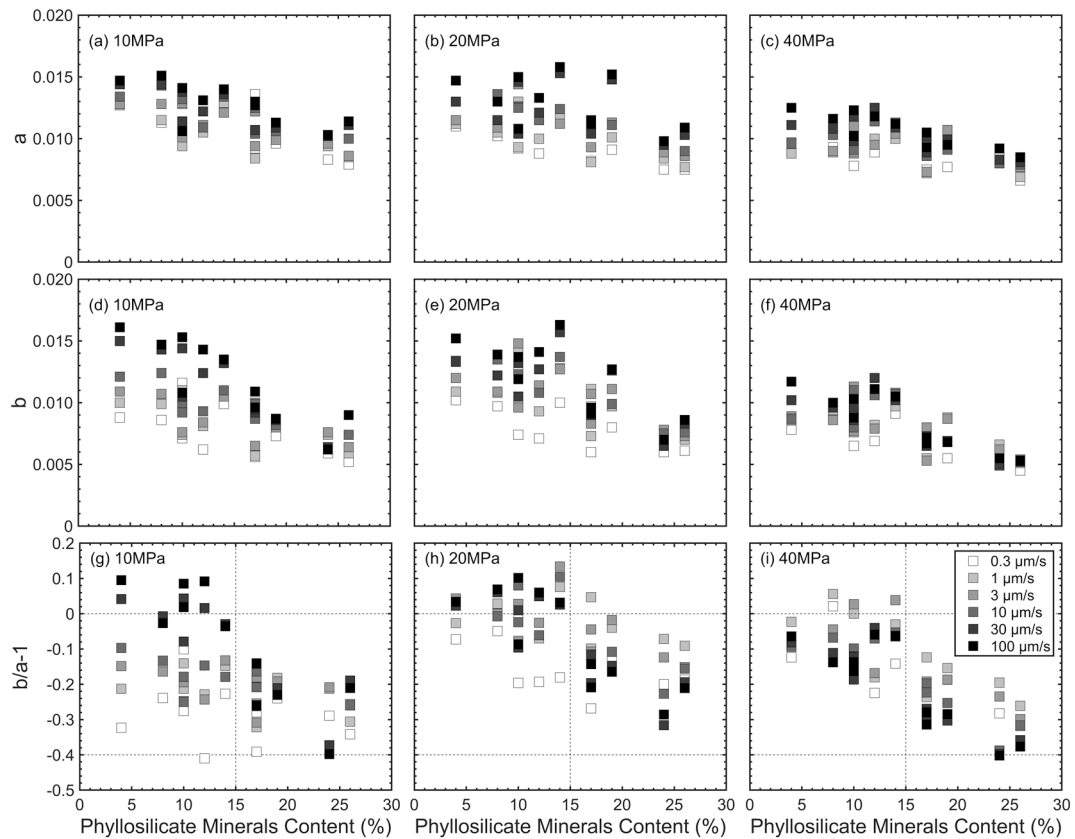


Figure 9. Friction constitutive parameters a , b and $(b/a - 1)$ as functions of phyllosilicate content at normal stresses of (a, d, and g) 10, (b, e, and h) 20, and (c, f, and i) 40 MPa. The legend shows the poststep velocity.

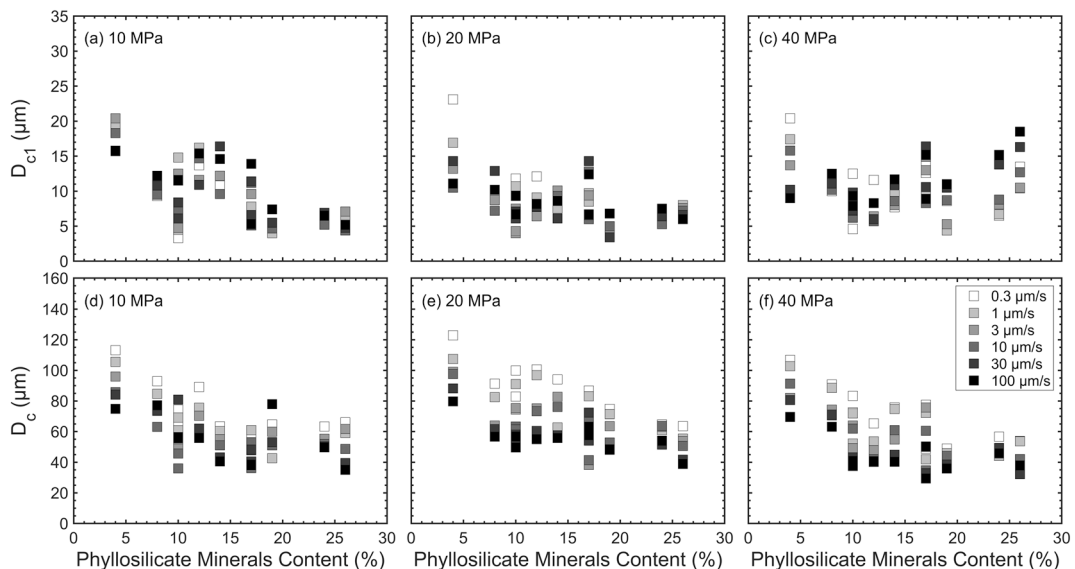


Figure 10. Slip evolution parameters (a–c) D_{c1} and (d–f) D_c against phyllosilicate mineral content at normal stresses of 10, 20, and 40 MPa. The legend shows the poststep velocity.

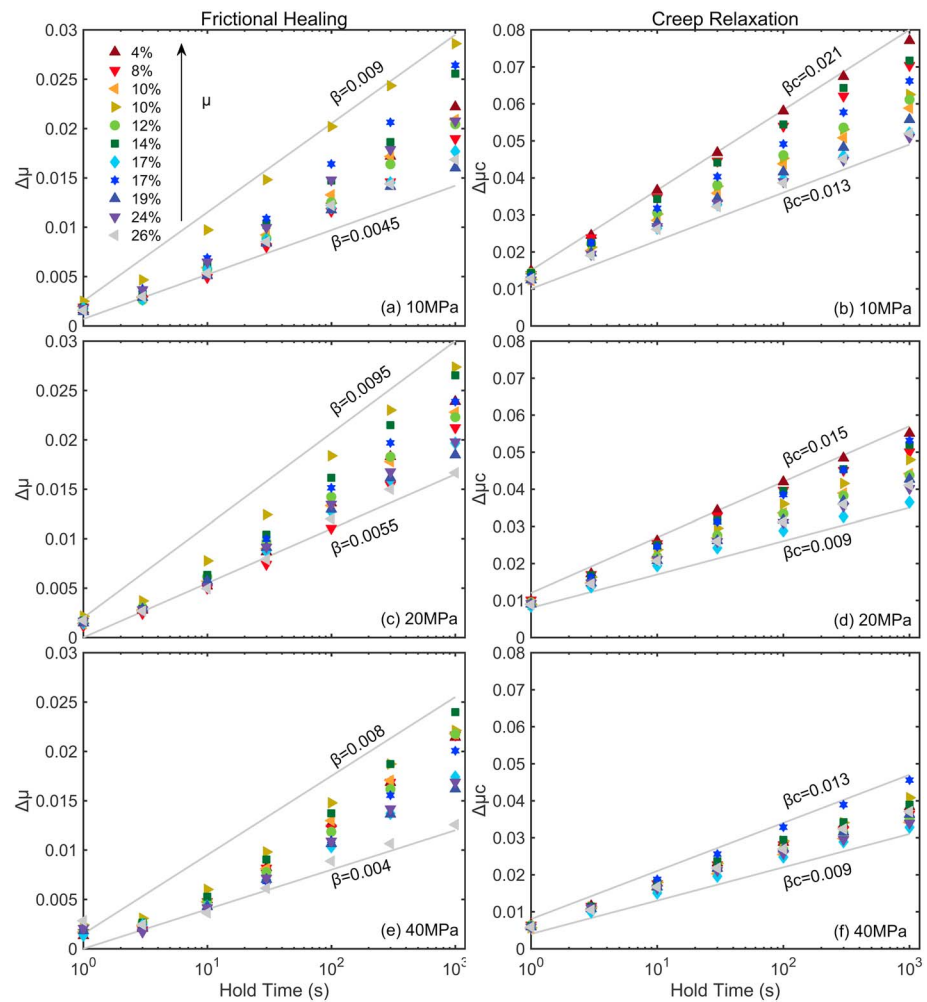


Figure 11. The frictional healing $\Delta\mu$ and relaxation $\Delta\mu_c$ as functions of the logarithm of hold time (t_h) at normal stresses of (a, b) 10, (c, d) 20, and (e, f) 40 MPa. The legend shows the phyllosilicate mineral content.

shearing velocities and the largest ($a - b$) values appear at the highest shearing velocity. Besides, unstable sliding can also be arrested if ($a - b$) transitions from negative to positive with increasing shear velocity (Shibazaki & Shimamoto, 2007), which appears at a normal stress of 40 MPa for samples containing <15 wt.% phyllosilicate minerals.

3.2. Friction Constitutive Parameters and Slip Evolution

In the RSF constitutive law, the value of a reflects the direct response of frictional strength upon the instantaneous change of shearing velocity, while the evolution of the state variables toward a new steady state is controlled by the value of b . The friction variables a , b , and $a - b$ are dependent not just on phyllosilicate content but also on microstructures, pore fluid pressure, and sliding velocity (Bos & Spiers, 2002; Chen et al., 2017; Niemeijer & Spiers, 2007; Scuderi & Collettini, 2016; Scuderi et al., 2017). The relationships of a and b (Table S2) and phyllosilicate mineral contents at normal stresses of 10, 20, and 40 MPa are shown in Figure 9. Values of a and b are in the range from 0 to 0.02, and the values at 40 MPa are lower than those at 10 and 20 MPa. We observe the strong dependence of both a and b on phyllosilicate content and shearing velocity. Values of a and b decrease monotonically with increased phyllosilicate contents and increase with shearing velocity. Our results are consistent with the observation that phyllosilicate-rich samples have lower a and b values than phyllosilicate-poor samples (Ikari, Niemeijer, & Marone, 2011).

The seismic response of crustal faults can be further divided into four categories (Boatwright & Cocco, 1996) according to the values of the product $(a - b)\sigma_n$, namely, strong seismic, weak seismic, compliant

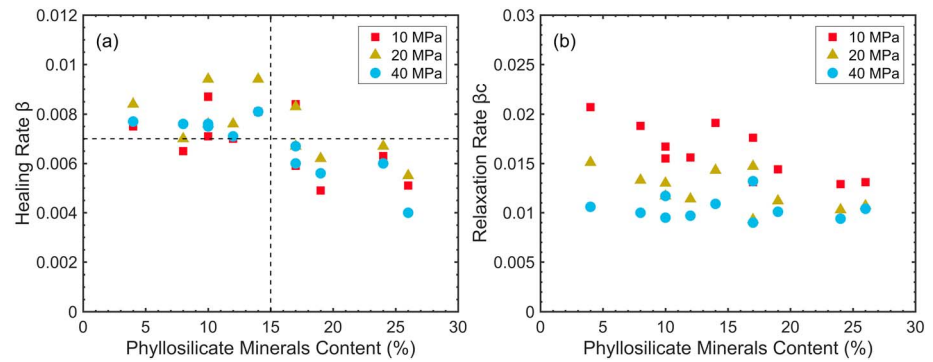


Figure 12. Relationships of (a) frictional healing rate β and (b) creep relaxation rate β_c with phyllosilicate mineral content at normal stresses of 10, 20, and 40 MPa.

(aseismic), and viscous (aseismic). To exclude the effect of normal stress (Zhang & He, 2013), we adopt the dimensionless parameter $(b/a - 1)$ to evaluate the sliding behavior of rock samples at different normal stresses. For fault gouge with $a - b < 0$ and $b/a - 1 < 0.2$, termed as weak seismic behavior, microseismic and intermittent dynamic slip behavior can be anticipated. We plot the dimensionless parameter $(b/a - 1)$ with phyllosilicate content (Figure 9) with most of the data < 0.2 . According to this classification, the samples lie in the region of weak seismic response where neither large stress drops nor episodic dynamic slip will occur. Similar to the trend of $(a - b)$ versus phyllosilicate content, the values of $(b/a - 1)$ decrease with increasing phyllosilicate content under different normal stresses.

The parameter D_c describes the characteristic distance for the full evolution of frictional response and is one fundamental parameter associated with preseismic slip and nucleation zones for mature faults (Marone & Kilgore, 1993). Since the twin state variable RSF law was employed to determine the friction parameters, we plot the relationship between both D_{c1} and D_c (Table S2) and phyllosilicate contents in Figure 10. Both values of D_{c1} and D_c decrease with an increase in phyllosilicate content at normal stresses of 10, 20, and 40 MPa. We do not observe a significant dependence of D_{c1} on shearing velocity at different normal stresses, while values of D_c are dependent on shearing velocity at higher normal stress.

3.3. Frictional Healing and Creep Relaxation

Frictional healing reflects the shear stress recovery following the stress drop and frictional relaxation is the result of both creep of fault materials and relaxation of the testing apparatus, both of which are vital in defining earthquake recurrence during interseismic slip (Carpenter, Collettini, et al., 2016, Im et al., 2017). The values of frictional healing $\Delta\mu$ and creep relaxation $\Delta\mu_c$ for these water-saturated samples depend both on the logarithm of hold time and phyllosilicate content (Figure 11). Higher values of frictional healing and creep relaxation can be found for samples containing lower phyllosilicate content and with longer hold times. We also observe the lowest values of frictional healing $\Delta\mu$ and creep relaxation $\Delta\mu_c$ at the highest normal stress, especially for $\Delta\mu_c$ at 40 MPa—where they range from 0 to 0.05 compared with those at 10 MPa where they range between 0 and 0.08.

The rates of frictional healing β and relaxation β_c are obtained (Table S3) by least squares fitting of the healing/relaxation-hold time curves (section 2.3) with these two parameters importantly associated with earthquake scaling (Im et al., 2017). The rate of frictional healing is an essential parameter controlling the features of fault rupture and interseismic stress drop (Heaton, 1990; Perrin et al., 1995; Scholz et al., 1986). Higher healing rates imply that the frictional strength necessary to prime fault rerupture is recovered rapidly during interseismic period, with an important impact on repeated seismic cycles (Ikari et al., 2014). Meanwhile, the earthquake afterslip results from the stress relaxation and thus the creep relaxation during a certain hold is associated with earthquake afterslip (Marone et al., 1991). In Figure 12, we observe that the healing rates are in the range of 0.004–0.010 and decrease with higher phyllosilicate contents. For samples with < 15 wt.% phyllosilicates, high healing rates ($\beta > 0.007$) are observed, whereas intermediate healing rates ($0.004 < \beta < 0.007$) are common for samples containing > 15 wt.% phyllosilicates. This trend is in good agreement with previous observations that phyllosilicate-rich samples show smaller magnitudes of healing

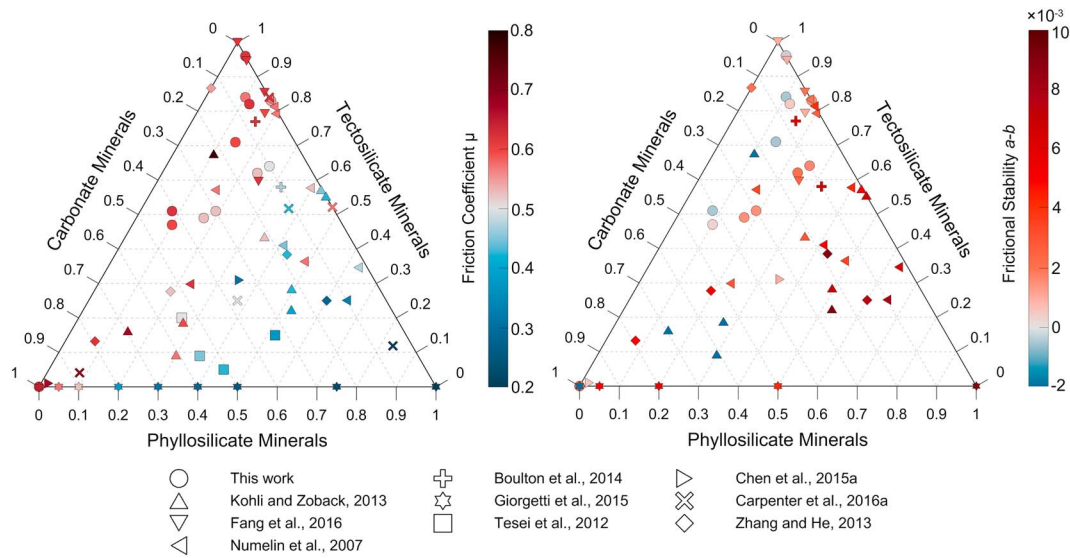


Figure 13. Comparisons of frictional strength and the frictional stability parameter ($a - b$) for samples of differing mineralogical compositions—including this work and previous studies (Boulton et al., 2014; Carpenter, Ikari, & Marone, 2016; Chen et al., 2015a; Fang et al., 2016; Giorgetti et al., 2015; Kohli & Zoback, 2013; Numelin et al., 2007; Tesei et al., 2012; Zhang & He, 2013). The color bars indicate the values of coefficient of friction and the parameter ($a - b$).

rates than those with tectosilicate-rich samples (Beeler et al., 2001; Carpenter, Collettini, et al., 2016). For the rates of creep relaxation, we also observe that relaxation rates increase with a decrease in normal stress. However, the mineralogic dependence of creep relaxation attenuates with the increase of normal stress.

4. Discussion

4.1. Dependence of Frictional Properties on Mineral Content

The frictional stability parameter ($a - b$) and the rates of frictional healing and creep relaxation are shown to scale with the frictional strength for the tested simulated fault gouges (Figures 6, 8, and 12). The fault gouges that exhibit higher frictional strength show negative values of ($a - b$) and high healing rates—which together promote potentially unstable sliding and seismic slip, relative to those samples that are frictionally weak (Figures 6, 7, and 12). Our experimental results demonstrate that the frictional properties of fault gouges from various reservoir rocks are significantly influenced by the phyllosilicate content (mostly white mica and chlorite in this study). Fault gouges dominated by tectosilicate (like quartz and feldspar) and carbonate (mainly calcite and dolomite) minerals show high frictional strength, while those containing higher proportions of phyllosilicates exhibit lower friction. Furthermore, in Figures 13 and 14, we place the observations of the frictional strength, frictional stability parameter ($a - b$) and frictional healing rates recovered in this work in the contexts of previous studies. These data imply that the three groups of minerals contribute differently to the frictional properties of fault gouge. For tectosilicate-rich and carbonate-rich minerals, we observe higher frictional strengths and velocity neutral to weakening behavior, contrary to phyllosilicate-rich minerals. However, negligible to low healing rates are common in phyllosilicate-rich samples and, in contrast, intermediate to high healing rates can be observed in carbonate-rich and tectosilicate-rich samples.

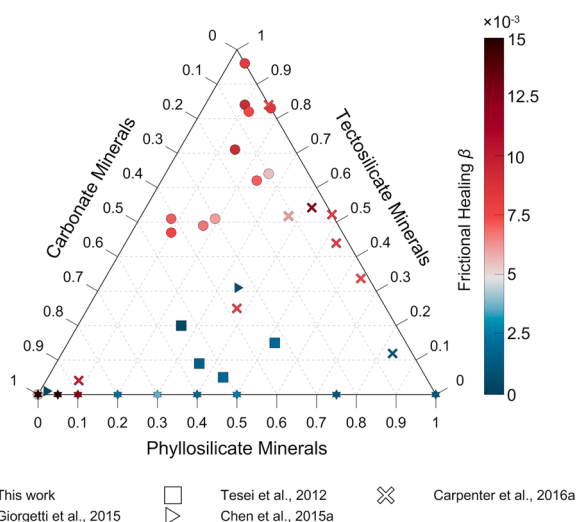


Figure 14. Ternary plot of mineral content showing rates of frictional healing for different mineral compositions and reporting this work and summarizing previous studies (Carpenter, Ikari, & Marone, 2016; Chen et al., 2015a; Giorgetti et al., 2015; Tesei et al., 2012). The color bar reflects the values of frictional healing rate β .

The role of mineralogy in defining frictional properties is partially illuminated by considering the impacts of frictional compaction and dilation (Marone, 1991). We plot normalized frictional compaction ($\Delta h_c/h$) and dilation ($\Delta h/h$) that evolves during holds for slide-hold-slide tests with

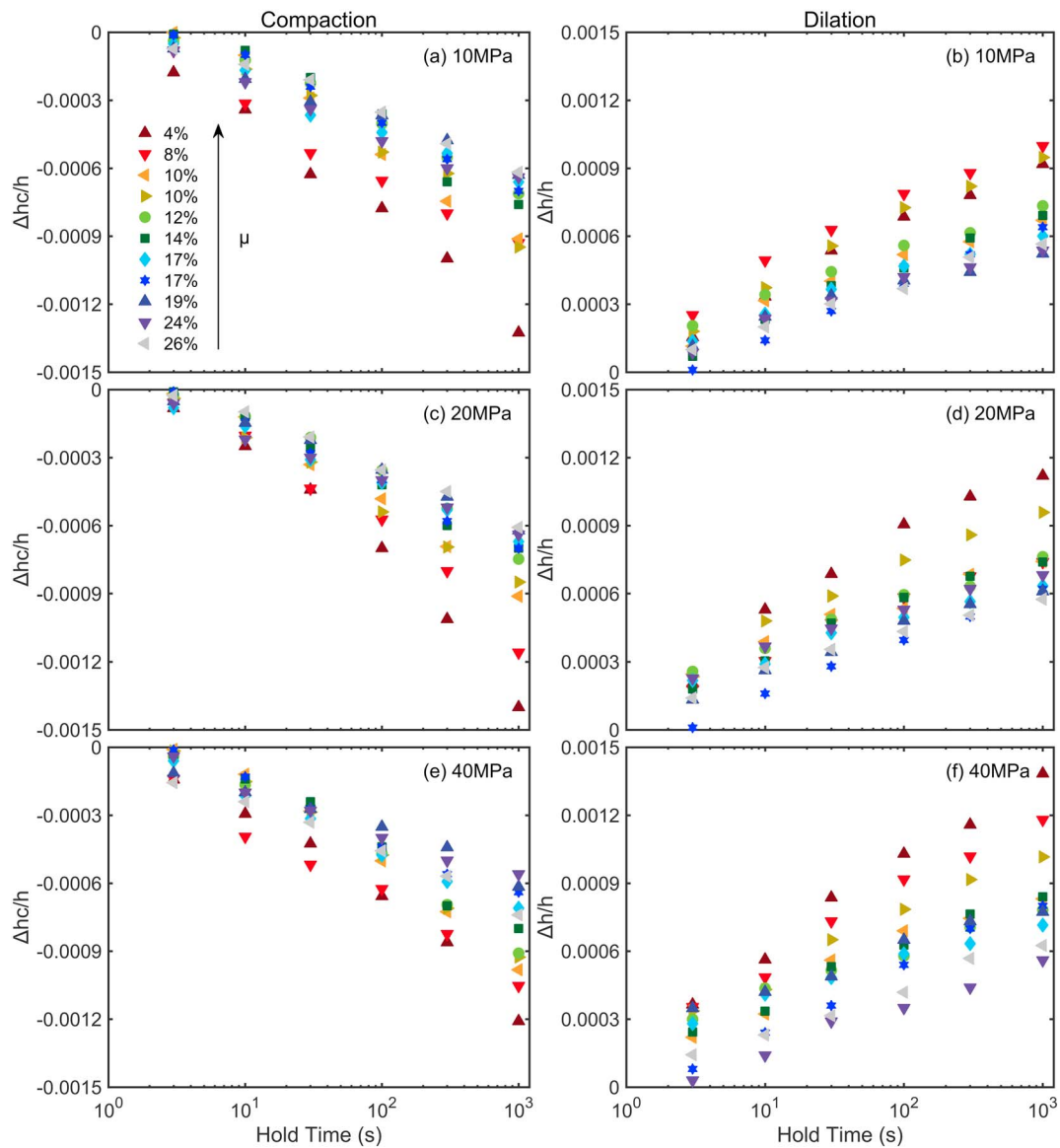


Figure 15. Normalized compaction ($\Delta h_c/h$) and dilation ($\Delta h/h$) for different hold times (t_h) at normal stresses of (a, b) 10, (c, d) 20, and (e, f) 40 MPa. The legend shows phyllosilicate content.

different hold times in Figure 15 (10, 20, and 40 MPa). Samples with higher friction coefficient compact and dilate the most, whereas the samples with higher phyllosilicate contents show lower compaction and dilation. Furthermore, the relationship between dilation rate and phyllosilicate content are plotted in Figure 16. The dilation rate decreases with increased phyllosilicate content with the phyllosilicate-rich samples showing the smallest dilation rate—this is attributed to the fact that the aligned phyllosilicate minerals can impact the grain-grain contacts in powders and thus minimize the effects of dilation (Numelin et al., 2007). Phyllosilicate-rich gouge samples show lower values of frictional dilation (Δh_c ; Figure 15) and dilation rates (Figure 16). This reflects that phyllosilicate-rich gouges have lower peak friction values and less strength loss upon reshear. Besides, the friction experiments indicate that the phyllosilicate-rich gouges show velocity strengthening behavior and lower healing rates. They will exhibit stable sliding once the driving stress exceeds their peak strength. On the contrary, phyllosilicate-poor gouge samples show higher values of frictional dilation and require more energy to reach higher peak friction values. Additionally, since the phyllosilicate-poor gouges exhibit velocity weakening behavior and

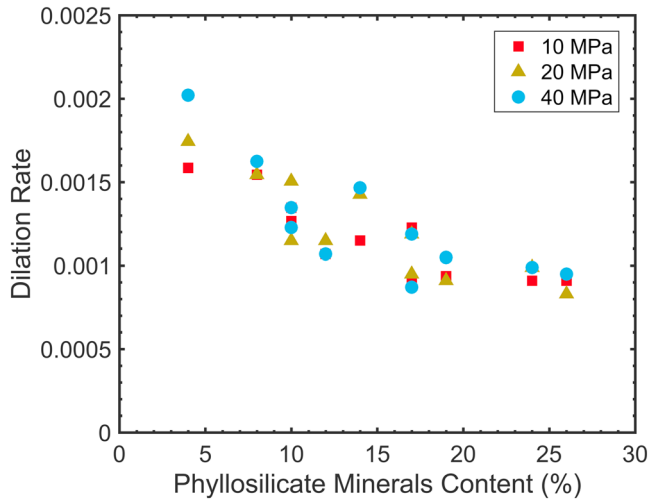


Figure 16. Scaling of dilation rate with phyllosilicate mineral content at normal stresses of 10, 20, and 40 MPa.

higher rates of healing, they will show unstable slip if sufficient driving stress exists to overcome peak strength and conditions of critical stiffness are met.

Carbonate minerals are key components in crustal rocks, and numerous previous studies indicate that the presence of carbonate minerals play an important role in the frictional stability and frictional healing response. For example, carbonate-rich fault gouge typically exhibits velocity strengthening or velocity neutral behavior at room temperatures (Scuderi et al., 2013) but may be driven to instability at higher temperatures (Verberne et al., 2013). “Non-Dieterich” healing behavior may exist in carbonate/clay fault gouge under hydrothermal conditions (Chen et al., 2015b), and calcite removal may change frictional stability behavior, even from velocity strengthening to velocity weakening behavior (Fang et al., 2016). Velocity strengthening behavior can also evolve into velocity weakening behavior at higher shearing velocity for carbonate-rich fault gouge (Carpenter, Ikari, et al., 2016).

To evaluate the effects of carbonate minerals, we first compare the frictional stability of sample CA-1 containing pure carbonates and sample VR-1 containing mostly tectosilicate minerals (Figure 17a). We only observe positive values of $(a - b)$ in the sample containing pure carbonates, indicating that the carbonate-rich fault gouge promotes velocity strengthening behavior under water-saturated conditions at room temperature (Carpenter, Ikari, et al., 2016; Scuderi et al., 2013). Negative values of $(a - b)$ exist for the sample containing nearly 100 wt.% tectosilicates and the values of $(a - b)$ in sample CA-1 are typically lower than those in sample VR-1 at normal stresses of 10, 20, and 40 MPa. Moreover, we compare the values of $(a - b)$ for samples containing the same phyllosilicate content but varied carbonate content. For example, the data at 20 MPa (Figure 17b) show that carbonate-poor fault gouge exhibits lower values of $(a - b)$ than carbonate-rich fault gouge (Fang et al., 2016).

The effects of carbonate minerals on fault frictional healing rates are discussed at a normal stress of 20 MPa. We compare the frictional healing rates of gouges containing the same content of phyllosilicates but different content of carbonates. It is observed that sample SA-2 (10 wt.% phyllosilicates, 6 wt.% carbonates) shows a higher healing rate than sample SH-1 (10 wt.% phyllosilicates, 42 wt.% carbonates; Table S3). This is different from Chen et al. (2015a; 68 wt.% calcite and 29 wt.% dolomite) and Carpenter, Collettini, et al. (2016; 86 wt.% carbonates) experimental results that the carbonate-rich samples show strong frictional healing and healing rates. This discrepancy could be mainly attributed to the influence of the tectosilicate minerals. The highest content of carbonates for the studied sandstones, shales and volcanic rock is about 42 wt.%, typically lower than that of 86 wt.% in the experiments of Carpenter, Collettini, et al. (2016).

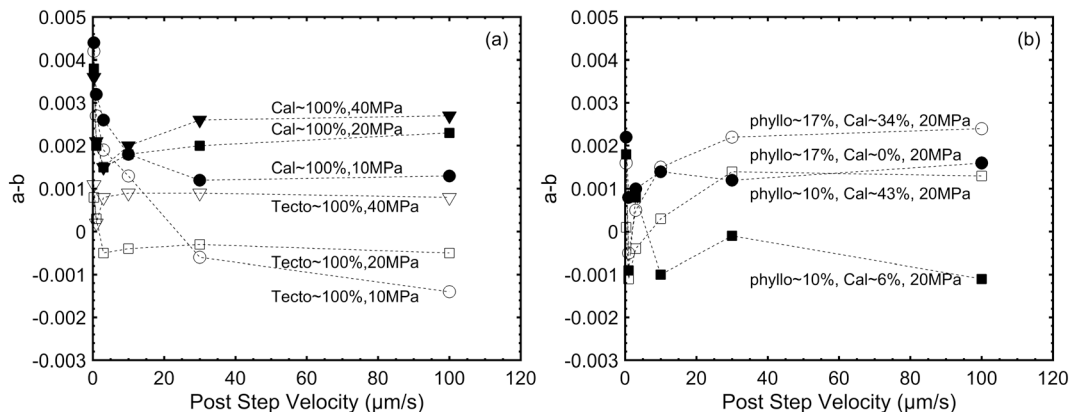


Figure 17. (a) Comparison of the frictional parameter $(a - b)$ between samples containing pure carbonate and tectosilicate minerals at normal stresses of 10, 20, and 40 MPa. (b) Comparison of frictional parameter $(a - b)$ between samples containing the same content of phyllosilicates but different carbonate contents.

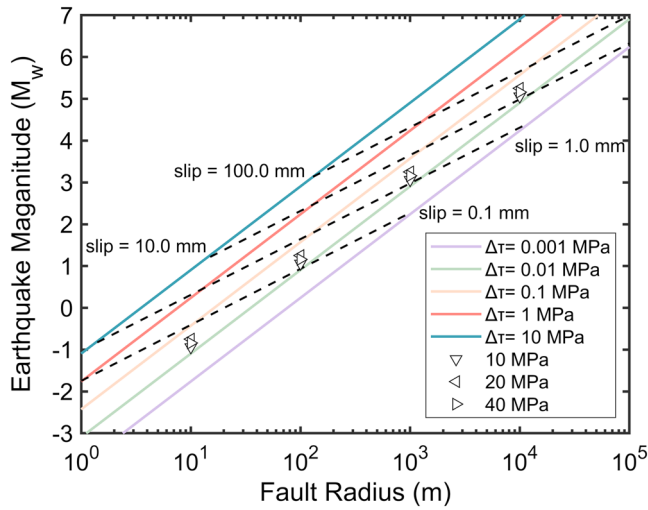


Figure 18. The relationship of earthquake moment magnitude (M_w) and fault radius (r) and corresponding slip offsets (modified from Zoback & Gorelick, 2012). The hollow triangles represent the data calculated from velocity step tests at 10, 20, and 40 MPa normal stress. Only maximum value of $(b - a)$ at every single normal stress is included. The velocity steps used for normal stresses of 10, 20, and 40 MPa are 30 to 100, 1 to 3, and 0.3 to 1 $\mu\text{m/s}$.

4.2. Implications for Seismicity From Lab Data

It is reported that stress drops recorded as a result of induced seismic events are of the same order of magnitude as those resulting from tectonic seismicity. Thus, the theoretical underpinnings for understanding tectonic earthquakes can be uniformly applied to induced earthquakes (Huang et al., 2017). On the basis of Brune's source model (Brune, 1970) and circular crack model (Vouillamoz et al., 2016), the relationship between seismic moment M_0 and stress drop $\Delta\tau$ can be expressed as

$$M_0 = \frac{16}{7} \Delta\tau \cdot r^3 \quad (9)$$

where r is the fault radius and $\Delta\tau$ is the stress drop and can be calculated from RSF theory as

$$\Delta\tau = \Delta\mu \cdot \sigma_n \quad (10)$$

$$\Delta\mu = |a - b| \ln\left(\frac{V_2}{V_1}\right) \quad (11)$$

where $\Delta\mu$ is the difference in the friction coefficient from before until after the stress drop. In RSF theory (section 2.3), the value of $\Delta\mu$ can be evaluated from equation (11) where σ_n is the normal stress applied normal to the fault. The earthquake magnitude (M_w) as a function by seismic moment (M_0) is defined by

$$M_w = \frac{2}{3} \log M_0 - 6. \quad (12)$$

As discussed previously, velocity weakening ($a - b < 0$) behavior only appears in samples with <15 wt.% phyllosilicate content—so we restrict our interest to those cases. By assuming a fault radius in the range from 10^1 to 10^4 m and characterizing unstable slip at normal stresses of 10, 20, and 40 MPa, we plot the relationship between seismic moment magnitude (M_w) and fault radius (r) and the corresponding slip distances (Fang et al., 2018; Zoback & Gorelick, 2012), as shown in Figure 18. We use the maximum value of $(b - a)$ data at every single normal stress in Figure 18 without differentiating different gouges. For the gouges studied, the maximum moment magnitudes at every single normal stress are similar and are in the range -2 to 5 with fault radii from 10^1 to 10^4 m. The calculated earthquake moment magnitude is thus a crucial parameter for seismic hazard evaluation and analysis during the lifetime of exploration of unconventional resources.

The moment magnitude (M_w) of induced earthquakes recorded in Oklahoma in 2011 peak at 5.7 (Keranen et al., 2014). Based on estimations of moment magnitudes from the stress drops in velocity stepping tests, the damaging moment magnitude (M_w) 5 events are possible when the fault radius is of the order $>10^4$ m. Under such circumstances, it is important to establish effective measures to avoid the occurrence of such higher moment magnitude events. For instance, as earthquake magnitudes scale with fault radius (Zoback & Gorelick, 2012), detailed and high-precision geologic surveys are essential for assessing the location and dimensions of preexisting faults. In addition, the above experimental results demonstrate that potentially unstable slips are observed in phyllosilicate-poor fault gouges and the stress drops increase with less phyllosilicate contents. The mineral compositions need to be evaluated for both the fault gouges and fault rocks to assess the seismic potential.

5. Conclusions

We report a systematic study of natural reservoir rocks from oil and gas reservoirs in China to investigate the effects of mineral composition on frictional strength, rate dependence, and frictional healing properties. We use velocity stepping and slide-hold-slide tests under water-saturated conditions at room temperature.

Empirical RSF theory and an iterative least squares approach are employed to determine friction constitutive parameters. We observe that the frictional properties of natural rock powders are strongly dependent on the content of phyllosilicate minerals. For the tested gouges (0 to 30 wt.% phyllosilicates), frictional strength decreases monotonically with increasing content of phyllosilicate minerals. Gouges samples with phyllosilicate content <15 wt.% exhibit velocity weakening behavior, potentially promoting unstable sliding, while those above this threshold show velocity strengthening behavior, promoting stable sliding and aseismic fault slip. The phyllosilicate-rich samples with intermediate healing rates would inhibit rapid dynamic reactivation during interseismic period, contrary to phyllosilicate-poor samples. We also observe a significant dependence of the frictional stability parameter ($a - b$) on both normal stress and shearing velocities. As common components in crustal rocks, carbonate minerals are shown to influence both the velocity dependence and time dependence of natural reservoir gouges.

By employing the RSF constitutive equations, we calculate the stress drops of fault slips by negative values of ($a - b$). Then, we link the stress drops observed in velocity step tests to the induced seismicity moment magnitude by referencing the method for calculating the moment magnitude of tectonic earthquakes. Meanwhile, the stress drops are closely correlated with the mineral compositions of the fault rocks and fault gouges. Our combined analysis provides insights into the potential moment magnitudes of earthquakes induced by oil and gas reservoir stimulation.

Acknowledgments

This research is supported by the National Natural Science Foundation of China under grants 41672268 and 41772286, and the U.S. Department of Energy (DOE) under Grant DE-FE0023354. The useful discussions with Chris Marone and Changrong He are also greatly appreciated. We thank the two reviewers for their insightful comments and instructive suggestions to improve the manuscript. The data for this paper are in the tables and the supporting information.

References

- Atkinson, G. M., Eaton, D. W., Ghofrani, H., Walker, D., Cheadle, B., Schultz, R., et al. (2016). Hydraulic fracturing and seismicity in the western Canada Sedimentary Basin. *Seismological Research Letters*, *87*(3), 631–647. <https://doi.org/10.1785/0220150263>
- Bakker, E., Hangx, S. J. T., Niemeijer, A. R., & Spiers, C. J. (2016). Frictional behaviour and transport properties of simulated fault gouges derived from a natural CO₂ reservoir. *International Journal of Greenhouse Gas Control*, *54*, 70–83. <https://doi.org/10.1016/j.ijggc.2016.08.029>
- Bao, X., & Eaton, D. W. (2016). Fault activation by hydraulic fracturing in western Canada. *Science*, *354*(6318), 1406–1409. <https://doi.org/10.1126/science.aag2583>
- Beeler, N. M., Hickman, S. H., & Wong, T. F. (2001). Earthquake stress drop and laboratory-inferred interseismic strength recovery. *Journal of Geophysical Research*, *106*(B12), 30,701–30,713. <https://doi.org/10.1029/2000JB900242>
- Beeler, N. M., & Tullis, T. E. (1997). The roles of time and displacement in velocity-dependent volumetric strain of fault zones. *Journal of Geophysical Research*, *102*(B10), 22,595–22,609. <https://doi.org/10.1029/97JB01828>
- Blanpied, M. L., Lockner, D. A., & Byerlee, J. D. (1995). Frictional slip of granite at hydrothermal conditions. *Journal of Geophysical Research*, *100*(B7), 13,045–13,064. <https://doi.org/10.1029/95JB00862>
- Blanpied, M. L., Marone, C. J., Lockner, D. A., Byerlee, J. D., & King, D. P. (1998). Quantitative measure of the variation in fault rheology due to fluid-rock interactions. *Journal of Geophysical Research*, *103*(B5), 9691–9712. <https://doi.org/10.1029/98JB00162>
- Boatwright, J., & Cocco, M. (1996). Frictional constraints on crustal faulting. *Journal of Geophysical Research*, *101*(B6), 13,895–13,909. <https://doi.org/10.1029/96JB00405>
- Bos, B., & Spiers, C. J. (2002). Frictional-viscous flow of phyllosilicate-bearing fault rock: Microphysical model and implications for crustal strength profiles. *Journal of Geophysical Research*, *107*(B2), 2028. <https://doi.org/10.1029/2001JB000301>
- Boulton, C., Moore, D. E., Lockner, D. A., Toy, V. G., Townend, J., & Sutherland, R. (2014). Frictional properties of exhumed fault gouges in DFDP-1 cores, Alpine Fault, New Zealand. *Geophysical Research Letters*, *41*, 356–362. <https://doi.org/10.1002/2013GL058236>
- Boulton, C., Yao, L., Faulkner, D. R., Townend, J., Toy, V. G., Sutherland, R., et al. (2017). High-velocity frictional properties of Alpine Fault rocks: Mechanical data, microstructural analysis, and implications for rupture propagation. *Journal of Structure Geology*, *97*, 71–92. <https://doi.org/10.1016/j.jsg.2017.02.003>
- Brune, J. N. (1970). Tectonic stress and the spectra of seismic shear waves from earthquakes. *Journal of Geophysical Research*, *75*(26), 4997–5009. <https://doi.org/10.1029/JB075i026p04997>
- Carpenter, B. M., Colletini, C., Viti, C., & Cavallo, A. (2016). The influence of normal stress and sliding velocity on the frictional behaviour of calcite at room temperature: Insights from laboratory experiments and microstructural observations. *Geophysical Journal International*, *205*(1), 548–561. <https://doi.org/10.1093/gji/ggw038>
- Carpenter, B. M., Ikari, M. J., & Marone, C. (2016). Laboratory observations of time-dependent frictional strengthening and stress relaxation in natural and synthetic fault gouges. *Journal of Geophysical Research: Solid Earth*, *121*, 1183–1201. <https://doi.org/10.1002/2015JB012136>
- Carpenter, B. M., Marone, C., & Saffer, D. M. (2009). Frictional behavior of materials in the 3D SAFOD volume. *Geophysical Research Letters*, *36*, L05302. <https://doi.org/10.1029/2008GL036660>
- Carpenter, B. M., Marone, C., & Saffer, D. M. (2011). Weakness of the San Andreas fault revealed by samples from the active fault zone. *Nature Geoscience*, *4*(4), 251–254. <https://doi.org/10.1038/ngeo1089>
- Chen, J., Niemeijer, A. R., & Spiers, C. J. (2017). Microphysically derived expressions for rate-and-state friction parameters, a , b , and D_c . *Journal of Geophysical Research: Solid Earth*, *122*, 9627–9657. <https://doi.org/10.1002/2017JB014226>
- Chen, J., Verberne, B. A., & Spiers, C. J. (2015a). Effects of healing on the seismogenic potential of carbonate fault rocks: Experiments on samples from the Longmenshan Fault, Sichuan, China. *Journal of Geophysical Research: Solid Earth*, *120*, 5479–5506. <https://doi.org/10.1002/2015JB012051>
- Chen, J., Verberne, B. A., & Spiers, C. J. (2015b). Interseismic re-strengthening and stabilization of carbonate faults by “non-Dieterich” healing under hydrothermal conditions. *Earth and Planetary Science Letters*, *423*, 1–12. <https://doi.org/10.1016/j.epsl.2015.03.044>
- Chung, F. H. (1973). Quantitative interpretation of X-ray diffraction patterns of mixtures. I. Matrix-flushing method for quantitative multicomponent analysis. *Journal of Applied Crystallography*, *7*(6), 519–525. <https://doi.org/10.1107/S0021889874010375>

- Crawford, B. R., Faulkner, D. R., & Rutter, E. H. (2008). Strength, porosity, and permeability development during hydrostatic and shear loading of synthetic quartz-clay fault gouge. *Journal of Geophysical Research*, *113*, B03207. <https://doi.org/10.1029/2006JB004634>
- Dieterich, J. H. (1978). Time-dependent friction and the mechanics of stick-slip. *Pure and Applied Geophysics*, *116*(4–5), 790–806. <https://doi.org/10.1007/BF00876539>
- Dieterich, J. H. (1979). Modeling of rock friction: 1. Experimental results and constitutive equations. *Journal of Geophysical Research*, *84*(B5), 2161–2168. <https://doi.org/10.1029/JB084iB05p02161>
- Ellsworth, W. L. (2013). Injection-induced earthquakes. *Science*, *341*(6142). <https://doi.org/10.1126/science.1225942>
- Fang, Y., den Hartog, S. A. M., Elsworth, D., Marone, C., & Cladouhos, T. (2016). Anomalous distribution of microearthquakes in the Newberry Geothermal Reservoir: Mechanisms and implications. *Geothermics*, *63*, 62–73. <https://doi.org/10.1016/j.geothermics.2015.04.005>
- Fang, Y., Elsworth, D., & Cladouhos, T. T. (2018). Reservoir permeability mapping using microearthquake data. *Geothermics*, *72*, 83–100. <https://doi.org/10.1016/j.geothermics.2017.10.019>
- Frye, K. M., & Marone, C. (2002). Effect of humidity on granular friction at room temperature. *Journal of Geophysical Research*, *107*(B11), 2309. <https://doi.org/10.1029/2001JB000654>
- Giorgetti, C., Carpenter, B. M., & Collettini, C. (2015). Frictional behavior of talc-calcite mixtures. *Journal of Geophysical Research: Solid Earth*, *120*, 6614–6633. <https://doi.org/10.1002/2015JB011970>
- Guglielmi, Y., Cappa, F., Avouac, J. P., Henry, P., & Elsworth, D. (2015). Seismicity triggered by fluid injection-induced aseismic slip. *Science*, *348*(6240), 1224–1226. <https://doi.org/10.1126/science.aab0476>
- Heaton, T. H. (1990). Evidence for and implications of self-healing pulses of slip in earthquake rupture. *Physics of the Earth and Planetary Interiors*, *64*(1), 1–20. [https://doi.org/10.1016/0031-9201\(90\)90002-F](https://doi.org/10.1016/0031-9201(90)90002-F)
- Hincks, T., Aspinall, W., Cooke, R., & Gernon, T. (2018). Oklahoma's induced seismicity strongly linked to wastewater injection depth. *Science*, *359*(6381), 1251–1255. <https://doi.org/10.1126/science.aap7911>
- Huang, Y., Ellsworth, W. L., & Beroza, G. C. (2017). Stress drops of induced and tectonic earthquakes in the central United States are indistinguishable. *Science Advances*, *3*(8). <https://doi.org/10.1126/sciadv.1700772>
- Hunfeld, L. B., Niemeijer, A. R., & Spiers, C. J. (2017). Frictional properties of simulated fault gouges from the seismogenic Groningen Gas Field under in situ P–T–chemical conditions. *Journal of Geophysical Research: Solid Earth*, *122*, 8969–8989. <https://doi.org/10.1002/2017JB014876>
- Ikari, M. J., Carpenter, B. M., Kopf, A. J., & Marone, C. (2014). Frictional strength, rate-dependence, and healing in DFD-1 borehole samples from the Alpine Fault, New Zealand. *Tectonophysics*, *630*, 1–8. <https://doi.org/10.1016/j.tecto.2014.05.005>
- Ikari, M. J., Marone, C., & Saffer, D. M. (2011). On the relation between fault strength and frictional stability. *Geology*, *39*(1), 83–86. <https://doi.org/10.1130/G31416.1>
- Ikari, M. J., Niemeijer, A. R., & Marone, C. (2011). The role of fault zone fabric and lithification state on frictional strength, constitutive behavior, and deformation microstructure. *Journal of Geophysical Research*, *116*, B08404. <https://doi.org/10.1029/2011JB008264>
- Ikari, M. J., Saffer, D. M., & Marone, C. (2007). Effect of hydration state on the frictional properties of montmorillonite-based fault gouge. *Journal of Geophysical Research*, *112*, B06423. <https://doi.org/10.1029/2006JB004748>
- Ikari, M. J., Saffer, D. M., & Marone, C. (2009). Frictional and hydrologic properties of clay-rich fault gouge. *Journal of Geophysical Research*, *114*, B05409. <https://doi.org/10.1029/2008JB006089>
- Im, K., Elsworth, D., Marone, C., & Leeman, J. (2017). The impact of frictional healing on stick-slip recurrence interval and stress drop: Implications for earthquake scaling. *Journal of Geophysical Research: Solid Earth*, *122*, 10,102–10,117. <https://doi.org/10.1002/2017JB014476>
- Karner, S. L., Marone, C., & Evans, B. (1997). Laboratory study of fault healing and lithification in simulated fault gouge under hydrothermal conditions. *Tectonophysics*, *277*(1–3), 41–55. [https://doi.org/10.1016/S0040-1951\(97\)00077-2](https://doi.org/10.1016/S0040-1951(97)00077-2)
- Keranen, K. M., Weingarten, M., Abers, G. A., Bekins, B. A., & Ge, S. (2014). Sharp increase in Central Oklahoma seismicity since 2008 induced by massive wastewater injection. *Science*, *345*(6195), 448–451. <https://doi.org/10.1126/science.1255802>
- Kohli, A. H., & Zoback, M. D. (2013). Frictional properties of shale reservoir rocks. *Journal of Geophysical Research: Solid Earth*, *118*, 5109–5125. <https://doi.org/10.1002/jgrb.50346>
- Leeman, J. R., Saffer, D. M., Scuderi, M. M., & Marone, C. (2016). Laboratory observations of slow earthquakes and the spectrum of tectonic fault slip modes. *Nature Communications*, *7*(1), –6. <https://doi.org/10.1038/ncomms11104>
- Lockner, D. A., Morrow, C., Moore, D., & Hickman, S. (2011). Low strength of deep San Andreas Fault gouge from SAFOD core. *Nature*, *472*(7341), 82–85. <https://doi.org/10.1038/nature09927>
- Lu, Z., & He, C. (2014). Frictional behavior of simulated biotite fault gouge under hydrothermal conditions. *Tectonophysics*, *622*, 62–80. <https://doi.org/10.1016/j.tecto.2014.03.002>
- Majer, E. L., Baria, R., Stark, M., Oates, S., Bommer, J., Smith, B., & Asanuma, H. (2007). Induced seismicity associated with enhanced geothermal systems. *Geothermics*, *36*(3), 185–222. <https://doi.org/10.1016/j.geothermics.2007.03.003>
- Marone, C. (1991). A note on the stress-dilatancy relation for simulated fault gouge. *Pure and Applied Geophysics*, *137*(4), 409–419. <https://doi.org/10.1007/BF00879042>
- Marone, C. (1998). The effect of loading rate on static friction and the rate of fault healing during the earthquake cycle. *Nature*, *391*(6662), 69–72. <https://doi.org/10.1038/34157>
- Marone, C., & Kilgore, B. (1993). Scaling of the critical slip distance for seismic faulting with shear strain in fault zones. *Nature*, *362*(6421), 618–621. <https://doi.org/10.1038/362618a0>
- Marone, C. J., Scholtz, C. H., & Bilham, R. (1991). On the mechanics of earthquake afterslip. *Journal of Geophysical Research*, *96*(B5), 8441. <https://doi.org/10.1029/91JB00275>
- Moore, D. E., & Lockner, D. A. (2011). Frictional strengths of talc-serpentine and talc-quartz mixtures. *Journal of Geophysical Research*, *116*, B01403. <https://doi.org/10.1029/2010JB007881>
- Morgan, J. K., & Boettcher, M. S. (1999). Numerical simulations of granular shear zones using the distinct element method: 1. Shear zone kinematics and the micromechanics of localization. *Journal of Geophysical Research*, *104*(B2), 2703–2719. <https://doi.org/10.1029/1998JB900056>
- National Energy Administration of China (2010). Analysis method for clay minerals and ordinary non-clay minerals in sedimentary rocks by the X-ray diffraction (SY/T 5163-2010). Petroleum Industry of China. [in Chinese]
- Niemeijer, A., Marone, C., & Elsworth, D. (2010). Fabric induced weakness of tectonic faults. *Geophysical Research Letters*, *37*, L03304. <https://doi.org/10.1029/2009GL041689>

- Niemeijer, A. R., & Spiers, C. J. (2007). A microphysical model for strong velocity weakening in phyllosilicate-bearing fault gouges. *Journal of Geophysical Research*, *112*, B10405. <https://doi.org/10.1029/2007JB005008>
- Numelin, T., Marone, C., & Kirby, E. (2007). Frictional properties of natural fault gouge from a low-angle normal fault, Panamint Valley, California. *Tectonics*, *26*, T02004. <https://doi.org/10.1029/2005TC001916>
- Paterson, M. S., & Wong, T. F. (2005). Experimental rock deformation—the brittle field. *Mineralogical Magazine*, *43*(326), 317.
- Perrin, G., Rice, J. R., & Zheng, G. (1995). Self-healing slip pulse on a frictional surface. *Journal of the Mechanics and Physics of Solids*, *43*(9), 1461–1495. [https://doi.org/10.1016/0022-5096\(95\)00036-1](https://doi.org/10.1016/0022-5096(95)00036-1)
- Reinen, L. A., & Weeks, J. D. (1993). Determination of rock friction constitutive parameters using an iterative least squares inversion method. *Journal of Geophysical Research*, *98*(B9), 15937. <https://doi.org/10.1029/93JB00780>
- Rosen, J. (2015). Huge study links wastewater injection wells to earthquakes. *Science*. <https://doi.org/10.1126/science.aac6857>
- Ruina, A. (1983). Slip instability and state variable friction laws. *Journal of Geophysical Research*, *88*(B12), 10,359–10,370. <https://doi.org/10.1029/JB088iB12p10359>
- Saffer, D. M., & Marone, C. (2003). Comparison of smectite- and illite-rich gouge frictional properties: Application to the updip limit of the seismogenic zone along subduction megathrusts. *Earth and Planetary Science Letters*, *215*(1–2), 219–235. [https://doi.org/10.1016/S0012-821X\(03\)00424-2](https://doi.org/10.1016/S0012-821X(03)00424-2)
- Samuelson, J., Elsworth, D., & Marone, C. (2009). Shear-induced dilatancy of fluid-saturated faults: Experiment and theory. *Journal of Geophysical Research*, *114*, B12404. <https://doi.org/10.1029/2008JB006273>
- Samuelson, J., & Spiers, C. J. (2012). Fault friction and slip stability not affected by CO₂ storage: Evidence from short-term laboratory experiments on North Sea reservoir sandstones and caprocks. *International Journal of Greenhouse Gas Control*, *11*, 78–90. <https://doi.org/10.1016/j.ijggc.2012.09.018>
- Scholz, C. H., Aviles, C., & Wesnousky, S. (1986). Scaling differences between large intraplate and interplate earthquakes. *Bulletin of the Seismological Society of America*, *76*(1), 65–70.
- Schultz, R., Atkinson, G., Eaton, D. W., Gu, Y. J., & Kao, H. (2018). Hydraulic fracturing volume is associated with induced earthquake productivity in the Duvernay play. *Science*, *359*(6373), 304–308. <https://doi.org/10.1126/science.aao0159>
- Schupp, R. W., & Drive, U. N. F. (2017). Hydraulic fracturing and its relationship to seismicity levels in Oklahoma, USA. *International Journal of Science Commerce and Humanities*, *5*, 50–59.
- Scuderi, M. M., Carpenter, B. M., & Marone, C. (2014). Physicochemical processes of frictional healing: Effects of water on stick-slip stress drop and friction of granular fault gouge. *Journal of Geophysical Research: Solid Earth*, *119*, 4090–4105. <https://doi.org/10.1002/2013JB010641>
- Scuderi, M. M., & Collettini, C. (2016). The role of fluid pressure in induced vs. triggered seismicity: Insights from rock deformation experiments on carbonates. *Scientific Reports*, *6*(1), 24852. <https://doi.org/10.1038/srep24852>
- Scuderi, M. M., Collettini, C., & Marone, C. (2017). Frictional stability and earthquake triggering during fluid pressure stimulation of an experimental fault. *Earth and Planetary Science Letters*, *477*, 84–96. <https://doi.org/10.1016/j.epsl.2017.08.009>
- Scuderi, M. M., Niemeijer, A. R., Collettini, C., & Marone, C. (2013). Frictional properties and slip stability of active faults within carbonate-evaporite sequences: The role of dolomite and anhydrite. *Earth and Planetary Science Letters*, *369*–370, 220–232. <https://doi.org/10.1016/j.epsl.2013.03.024>
- Shapiro, S. A., Dinske, C., & Rothert, E. (2006). Hydraulic-fracturing controlled dynamics of microseismic clouds. *Geophysical Research Letters*, *33*, L14312. <https://doi.org/10.1029/2006GL026365>
- Shibazaki, B., & Shimamoto, T. (2007). Modelling of short-interval silent slip events in deeper subduction interfaces considering the frictional properties at the unstable-stable transition regime. *Geophysical Journal International*, *171*(1), 191–205. <https://doi.org/10.1111/j.1365-246X.2007.03434.x>
- Takahashi, M., Mizoguchi, K., Kitamura, K., & Masuda, K. (2007). Effects of clay content on the frictional strength and fluid transport property of faults. *Journal of Geophysical Research*, *112*, B08206. <https://doi.org/10.1029/2006JB004678>
- Tembe, S., Lockner, D. A., & Wong, T.-F. (2010). Effect of clay content and mineralogy on frictional sliding behavior of simulated gouges: Binary and ternary mixtures of quartz, illite, and montmorillonite. *Journal of Geophysical Research*, *115*, B03416. <https://doi.org/10.1029/2009JB006383>
- Tesei, T., Collettini, C., Carpenter, B. M., Viti, C., & Marone, C. (2012). Frictional strength and healing behavior of phyllosilicate-rich faults. *Journal of Geophysical Research*, *117*, B09402. <https://doi.org/10.1029/2012JB009204>
- Togo, T., Yao, L., Ma, S., & Shimamoto, T. (2016). High-velocity frictional strength of Longmenshan fault gouge and its comparison with an estimate of friction from the temperature anomaly in WFS-1 drill hole. *Journal of Geophysical Research: Solid Earth*, *121*, 5328–5348. <https://doi.org/10.1002/2016JB012880>
- Verberne, B. A., Niemeijer, A. R., De Bresser, J. H. P., & Spiers, C. J. (2015). Mechanical behavior and microstructure of simulated calcite fault gouge sheared at 20–600 °C: Implications for natural faults in limestones. *Journal of Geophysical Research: Solid Earth*, *120*, 8169–8196. <https://doi.org/10.1002/2015JB012292>
- Verberne, B. A., Spiers, C. J., Niemeijer, A. R., De Bresser, J. H. P., De Winter, D. A. M., & Plümper, O. (2013). Frictional properties and microstructure of calcite-rich fault gouges sheared at sub-seismic sliding velocities. *Pure and Applied Geophysics*, *171*(10), 2617–2640. <https://doi.org/10.1007/s00024-013-0760-0>
- Vouillamoz, N., Wust Bloch, G. H., Abednego, M., & Mosar, J. (2016). Optimizing event detection and location in low-seismicity zones: Case study from Western Switzerland. *Bulletin of the Seismological Society of America*, *106*(5), 2023–2036. <https://doi.org/10.1785/0120160029>
- Vrolijk, P., & van der Pluijm, B. A. (1999). Clay gouge. *Journal of Structural Geology*, *21*(8–9), 1039–1048. [https://doi.org/10.1016/S0191-8141\(99\)00103-0](https://doi.org/10.1016/S0191-8141(99)00103-0)
- Walsh, F. R., & Zoback, M. D. (2015). Oklahoma's recent earthquakes and saltwater disposal. *Science Advances*, *1*(5). <https://doi.org/10.1126/sciadv.1500195>
- Yeck, W. L., Hayes, G. P., McNamara, D. E., Rubinstein, J. L., Barnhart, W. D., Earle, P. S., & Benz, H. M. (2017). Oklahoma experiences largest earthquake during ongoing regional wastewater injection hazard mitigation efforts. *Geophysical Research Letters*, *44*, 711–717. <https://doi.org/10.1002/2016GL071685>
- Zhang, L., & He, C. (2013). Frictional properties of natural gouges from Longmenshan fault zone ruptured during the Wenchuan M_w 7.9 earthquake. *Tectonophysics*, *594*, 149–164. <https://doi.org/10.1016/j.tecto.2013.03.030>
- Zoback, M. D., & Gorelick, S. M. (2012). Earthquake triggering and large-scale geologic storage of carbon dioxide. *Proceedings of the National Academy of Sciences*, *109*(26), 10,164–10,168. <https://doi.org/10.1073/pnas.1202473109>